



# Simultaneous application of soot and temperature measurements in a pressurized turbulent flame by laser-induced incandescence and coherent anti-Stokes Raman scattering for particle sizing

Klaus Peter Geigle<sup>1</sup> · Hannah Scheffold<sup>1</sup> · Patrick Nau<sup>1</sup> · Zhiyao Yin<sup>1</sup>

Received: 26 January 2023 / Accepted: 18 April 2023 / Published online: 27 April 2023  
© The Author(s) 2023

## Abstract

Simultaneous application of multi-channel laser-induced incandescence (LII) and shifted vibrational coherent anti-Stokes Raman scattering (SV-CARS) to study sooting flames is demonstrated for the first time. The potential of this diagnostics combination is evaluated on the basis of characterization of soot particles and correlation of soot presence with temperature. For that purpose, a sooting swirl flame operated at three bars has been employed with ethylene as fuel. The novel combination of CARS and time-resolved LII (TiRe LII) enables the estimation of particle size and correlation of this quantity with local gas temperature; simultaneously acquired 2D LII images provide information on the soot distribution in the ambience of the measurement volume which is used by CARS and TiRe LII. Even if the used LII model is approximative in some respect, the detected LII decay times indicate very small particle size throughout the flame relative to an atmospheric laminar diffusion flame which was used for comparison. In most instances, soot presence relates to local gas temperatures in a range between 1600 and 2400 K. Rare soot events at cooler temperatures occur near the nozzle exit and are attributed to transported soot. Comparison of the peak soot temperatures during the LII process shows a significant decrease in the turbulent pressurized flame relative to the laminar atmospheric reference flame. This is attributed to a less-efficient LII heat-up process at turbulent pressurized conditions due to beam steering. The background blackbody temperature, which can be derived by evaluating the signal captured in the different color channels of the LII system towards the end of the LII process, has been identified to be mostly controlled by hotter soot filaments between the laser plane and the detector. Thus, the LII signal tail is not a good measure of the local gas temperature in the measurement volume for this type of configuration.

## 1 Introduction

The climate effect of non-CO<sub>2</sub> emissions from aero-engines is under strong debate [1]. This is accompanied by increasingly stringent legislation of the respective combustion systems, which will include a threshold for particle number in the future in addition to the traditional limits for total particle mass [2]. Consequently, design procedures for future combustors will have to consider soot particle number—related to size—which essentially drives combustion simulation to account for particle size. Appropriate simulation tools for turbulent pressurized combustion have only

recently started to incorporate particle sizes or size distributions [3, 4]. Consequently, an estimate of particle sizes by in situ soot particle measurements in semi-technical flames is required to validate those models. Estimation of particle size in flames frequently relies on time-resolved LII (TiRe LII) tracking the signal decay, which can be realized as point measurement with photomultipliers (PMTs) [5, 6] or few or multiple exposures on 2D image intensified cameras [7–10]. Tian et al. extended the approach of shifting the camera gate by adding a second color channel and evaluating the pyrometrically derived particle temperature decay instead of the LII signal, thereby improving accuracy [11]. Only rarely, this concept has been applied to pressurized flames, and if so, mainly to laminar cases [12, 13]. LII modelling specifically for pressurized cases has, for example, been detailed in [14, 15]. Combination of particle sizing with temperature measurements is feasible by combining 2D TiRe LII with non-linear excitation regime two-line atomic fluorescence (NTLAF) [16]. Here, the advantage is the derivation of

✉ Klaus Peter Geigle  
klauspeter.geigle@dlr.de

<sup>1</sup> Institute of Combustion Technology, German Aerospace Center (DLR), Pfaffenwaldring 38-40, 70569 Stuttgart, Germany

2D maps of both quantities particle size and temperature as demonstrated for various atmospheric turbulent flames. However, in those cases, particle sizing relies on only few ICCD exposures, and NTLAF has a limited range of application for cold or oxidative conditions.

With this paper, we present a different approach by developing an optical scheme to combine CARS and LII, where CARS provides additional information on the gas temperature in the ambience of the LII-heated soot particles. As a test case, we chose a pressurized sooting swirl flame similar to those that have been studied by various diagnostics in the past, including OH, PAH and fuel tracer LIF, quantitative LII, CARS, PIV and combination of kHz imaging diagnostics [17–23].

The so-far generated dataset has been used extensively by modelers from academia and industry in the framework of the International Sooting Flame Workshop series [24]. With the current measurements, we provide complementary information to support the understanding of soot formation in that type of flames, even if the derived data show some uncertainty due to assumptions in the used LII model and the turbulent-stochastic nature of the studied flame and deviations of the exact flame conditions. Qualitatively, estimated particle sizes indicate presence of quite young soot in the flame, which compares well with particle sizes derived from detailed soot modelling following the approach published in [4, 25–29].

## 2 Combustor setup

The burner has initially been designed and characterized within the European project FIRST (Fuel Injector Research for Sustainable Transport), and therefore is named FIRST combustor or pressurized sooting swirl flame. As already described in [18], it consists of three concentric nozzles. Air at room temperature is supplied to the flame through a central (diameter 12.3 mm) and an annular nozzle (inner diameter 14.4 mm, outer diameter 19.8 mm). The air flows are fed from separate plenums and pass radial swirlers consisting of 8 channels (width  $w = 4.2$  mm, height  $h = 5.4$  mm, swirl number  $S = 0.82$  and swirl angle  $\alpha_m = 40.5^\circ$  following the calculation in [30] for the central nozzle and 12 channels ( $w = 3.2$  mm,  $h = 4.5$  mm,  $S = 0.79$ ,  $\alpha_m = 38.6^\circ$ ) for the annular nozzle. Gaseous fuel ( $C_2H_4$ ) is injected in between both air flows through 60 straight channels ( $0.5 \times 0.4$  mm<sup>2</sup>) forming a concentric ring. This fuel placement mimics the atomizing lip between swirled air flows as used for spray flames. The exit planes of the fuel and air nozzles are located at the level of the combustion chamber inlet, defined as height  $h = 0$ . This allows full optical access to the fuel injection. The combustion chamber measures 120 mm in height and has a square cross section of  $68 \times 68$  mm<sup>2</sup> with beveled edges

(see Fig. 1). Four 3-mm-thick quartz windows ( $127 \times 59$  mm<sup>2</sup>) are mounted between four water-cooled metal posts, yielding excellent optical access of  $51.4 \times 120$  mm<sup>2</sup> to the flame. The water-cooled top plate has a cylindrical exhaust hole (diameter 40 mm, length 24 mm), linked to the combustion chamber by a curved transition. The high velocity in the exhaust tube prevents any backflow from outside the combustion chamber. An additional hole of 6 mm diameter positioned off-axis, serving to record the dynamic pressure of lean, thermo-acoustically active flames [31] via a probing pipe, had not been blocked due to an oversight, which resulted in slightly different flame conditions compared to [17–23]. Each of the corner posts has an additional air duct of 5 mm diameter for the injection of secondary air into the combustor at a height of 80 mm. The four radially injected jets meet on the combustor axis and form a stagnation point. A metal plate shields the burner front plate from the hot combustion gases during operation. This is required because of the lack of external cooling of this part.

The combustor is mounted in a water-cooled pressure housing with large optical access ( $60 \times 120$  mm<sup>2</sup>) from 4 sides. The pressure can be adjusted by partially blocking the exhaust port with a movable piston. An air flow through the gap between the combustion chamber and the pressure housing serves as air cooling for the windows of the combustion chamber. The inner surface of the combustor windows does not show severe degradation during operation, but exhibits some soot deposition at certain operating conditions.

The combustor was designed for operation at approximately 10 kW/bar thermal power providing Re numbers

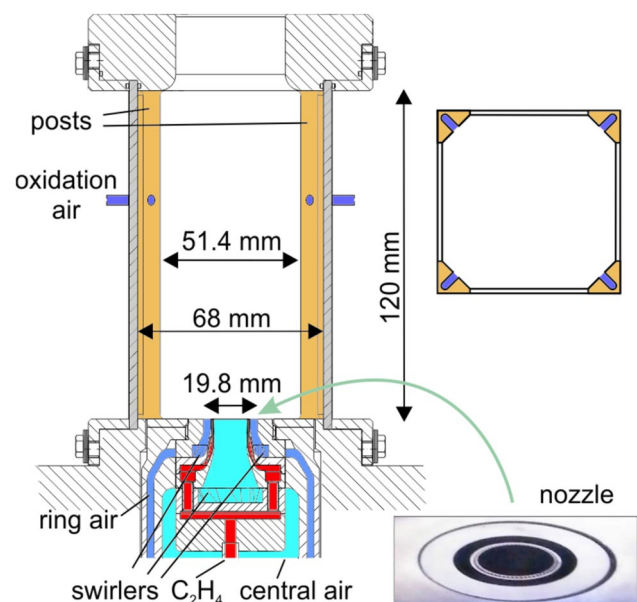


Fig. 1 FIRST combustor to stabilize sooting pressurized swirl flames

clearly above 10,000. The flow rates applied for the presented study are shown in Table 1, which is one of the cases listed in [17], differing only in the open probing hole mentioned above. The air and fuel flows were controlled using electronic mass flow controllers (Bronkhorst), which were carefully calibrated in-house; the accuracy of the calibration is estimated to be below 1% of the maximum flow rates. The equivalence ratio  $\phi$  and thermal power  $P$  were calculated from the primary air flow rate  $Q_{\text{air}}$  as a sum of central ( $Q_{\text{air,c}}$ ) and ring air ( $Q_{\text{air,r}}$ ), whereas the global equivalence ratio  $\phi_{\text{global}}$  and the global thermal power  $P_{\text{global}}$  were calculated from the total air flow rate,  $Q_{\text{air}} + Q_{\text{oxi}}$ . The amount of oxidation air is given as fraction  $Q_{\text{oxi}}/Q_{\text{air}}$ . Note that due to the excess fuel, the value for  $P$  is limited by the combustion air mass flow in most cases, whereas  $\phi_{\text{global}}$  becomes lean after injection of oxidation air and thus  $P_{\text{global}}$  depends on the fuel mass flow. The air split ratio is defined as the ratio of central air to the total combustion air  $Q_{\text{air,c}}/Q_{\text{air}}$ . For this ratio, a value of 0.3 is chosen. For higher values, the sooting region shifts towards the flame periphery, leading to increased soot deposition on the inner surface of the combustion chamber windows.

In the current experiments, we found CARS temperatures somewhat deviating from those reported in 2014 [18] despite a very similar visual impression of the flame, which is attributed to the accidentally open probing hole top of the combustor. An additional outflow relative to the reference conditions in previous publications sensitively affects the balance of upstream and downstream flow of the secondary air injection in the position where those four jets meet close to the combustor axis. The full data set derived with various diagnostics between 2013 and 2015 [17–19] includes both qualitative and quantitative characterizations of the sooting processes in these flames and is therefore considered self-consistent. However, as we varied the equivalence ratio in steps of 0.1, which did not result in significant changes in derived particle sizes, we consider our results as qualitatively reliable and representative of previously studied cases. Given the known uncertainties of deducing particle sizes from the LII signal decay behavior, which are detailed below, we are nevertheless able to provide an estimate of size range and sensitivities of this quantity to the operating conditions. For model validation purposes, even this relatively coarse information could prove invaluable for modelers.

An atmospheric laminar diffusion flame, originally presented in [32], was used for the development of the combined diagnostics and initial tests. Settings and detailed characterization of the so-called Gülder flame is available in [32] and all preceding publications referring to that original one. The flame of roughly 65 mm visible height features soot volume fractions up to about 7–8 ppm at very stable conditions and therefore is a good proxy for some soot luminosity, which is also present in the pressurized turbulent flame. The location defined as reference by the LII workshop community [33] is on centerline at 42 mm above the fuel pipe, where the soot properties are relatively invariant with location.

### 3 Optics setup

#### 3.1 Diagnostics combination

One of the reasons that, so far, a combination of LII and CARS has only once been demonstrated in literature for a different purpose [34], is the challenge of merging the different types of excitation and detection configurations for both diagnostics. This is reflected by the following three major challenges: (a) the configuration of the respective excitation and detection schemes, i.e. inherently different characteristics of geometrical setup, (b) a sufficiently small CARS measurement volume, and (c) the need to shift both measurement volumes synchronously relative to the fixed high-pressure facility. Main requirements as visualized in Fig. 2 are (a) a synchronous movement of the CARS and LII excitation optics, where the LII beam must pass the large CARS optics due to optical constraints and (b) a synchronous translation of the receiver optics for CARS and TiRe LII, both using fiber optics, but also a set of additional optics.

In our setup, the focusing lens for CARS had been predefined as this is the closest possible to the measurement location, thus provides the shortest CARS measurement volume. When combined with a cylindrical lens ( $f = -20$  mm, in the IR excitation beam only), positioned in fixed distance to the spherical  $f = 250$  mm lens, this setup allows for exciting the LII process in the same location as the CARS measurement and additional 2D LII imaging through the remaining optical access to the combustor. Consequently,

**Table 1** Nominal flame parameters for the studied flame: Pressure,  $p$ , flow rates for air through burner (central and ring),  $Q_{\text{air,c}}$  and  $Q_{\text{air,r}}$ , fuel,  $Q_{\text{fuel}}$ , oxidation air through secondary air inlet,  $Q_{\text{oxi}}$ , equivalence

ratios,  $\phi$ ,  $\phi_{\text{global}}$ , thermal powers,  $P$ ,  $P_{\text{global}}$ , and fractions  $Q_{\text{air,c}}/Q_{\text{air}}$  and  $Q_{\text{oxi}}/Q_{\text{air}}$  with  $Q_{\text{air}} = Q_{\text{air,c}} + Q_{\text{air,r}}$

$P$ [bar]	$\phi$	$P_{\text{primary}}$ [kW]	$Q_{\text{air,c}}$ [slm]	$Q_{\text{air,r}}$ [slm]	$Q_{\text{fuel}}$ [slm]	$Q_{\text{oxi}}$ [slm]	$Q_{\text{air,c}}/Q_{\text{air}}$	$Q_{\text{oxi}}/Q_{\text{air}}$	$\phi_{\text{global}}$	$P_{\text{global}}$ [kW]	Case
3	1.2	32.2	140.8	328.5	39.3	187.4	0.3	0.4	0.86	38.6	1.2ox

Flow rates in standard liters per minute (slm) are referenced to 1.013 bar and 273 K

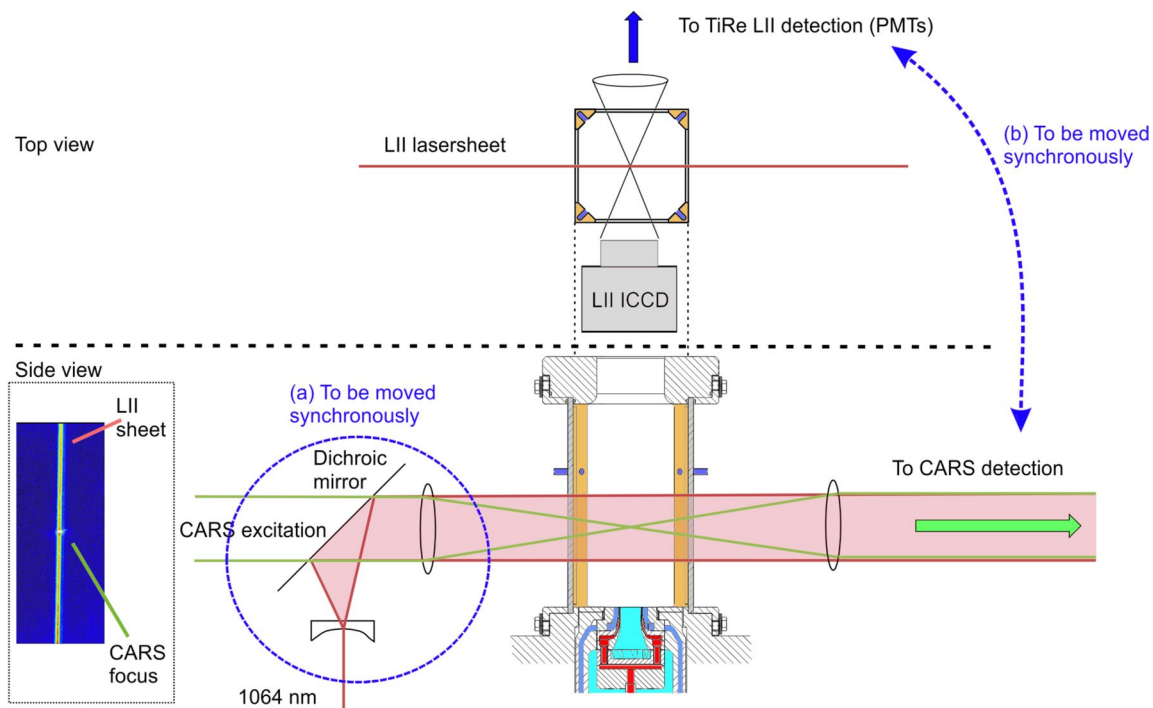


**Fig. 2** Setup for simultaneous LII and CARS measurements

the LII laser sheet overlaps with the CARS measurement volume at the focal point of the spherical lens by alignment of both along the same axis (see Fig. 2, left). CARS and LII excitation beam (and sheet, respectively), are combined with a dichroic mirror at fixed distance from the CARS focusing lens. The overlap of LII and CARS detection volumes was determined with a beam profiler and a pin-hole target placed inside the combustor. Typically, 1200 laser pulse pairs for LII and CARS have been used for the locations in the turbulent flame. This number could be reduced to 100 for the laminar case.

### 3.2 LII specifics

Soot particle heat-up was done using a 10 Hz pulsed Nd:YAG laser (Brilliant B, Quantel) at 1064 nm with a pulse duration of 9 ns and the optics described above. LII signals were collected normal to the excitation beam. To optimize signal collection efficiency for TiRe LII signal, the detection path is inclined by about  $11^\circ$ , i.e. not clipped by the window flange for the lowest measurement locations. Using an aluminium mirror, it is directed towards the translation stage occupied by the CARS receiver optics, where it is coupled into an optical fiber. The used large achromatic optics ( $f=160$  mm, diameter = 80 mm) provides roughly a 1:1 image onto the fiber entrance of 1 mm diameter. Thus, the LII measurement volume is 1 mm large and roughly 0.2 mm thick (thickness of the laser sheet). The pulse energy of the

LII laser beam is typically measured before the sheet optics due to spatial constraints; any part of the IR beam remaining in the CARS detection pathway is separated by a dichroic mirror and dumped.

The exit side of the used 1000  $\mu\text{m}$ -diameter fiber is connected to a detection unit similar to that described in [5]. The optical mount system for the detection optics features a filter wheel for variable signal attenuation with a set of carefully selected, spectrally relatively flat neutral density filters, two dichroic beam splitters at 605 and 740 nm (Semrock, FF605-Di02 and FF740-Di01, respectively) and three gated PMTs (Hamamatsu, H11526-20 NF) equipped with specific band pass filters (Semrock, FF01-500/24, FF02-684/24 and FF01-800/12, respectively). The optical detection path including achromatic lens, fiber, filter combinations and detectors is characterized with a suitable light source coupled to an integrating sphere placed close to the pressure housing. The spectral arrangement of filters is shown in Fig. 3, the PMT sensor at 684 nm has not been used for derivation of the particle temperature during the LII process. This is because we realized that this PMT had a sufficiently different temporal response compared to the other two PMTs (identical type, different year of production), which caused physically unreasonable temperatures especially in the beginning of the decay curve where steep temporal gradients prevail. It has been shown for phosphor thermometry that different PMTs or even using a different oscilloscope channel can result in different decay times [35]. Because the decay rates in the

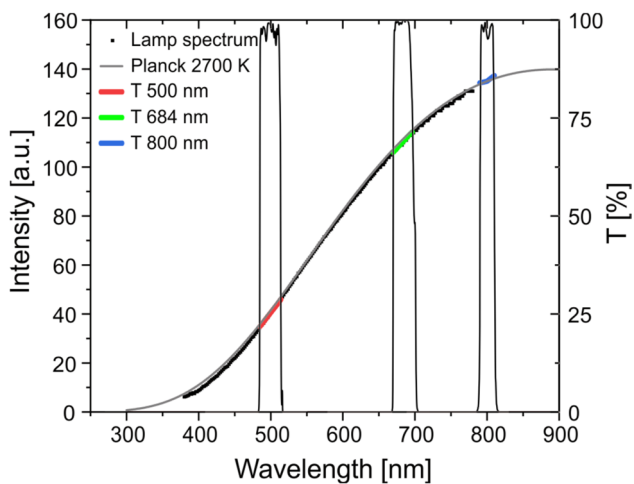


**Fig. 3** Spectrum of the calibration lamp and used filter intervals

investigated flames were rather short, it was not possible to exclude the beginning of the curve, which was mostly affected by the mentioned effect. Therefore, we used only those two of the PMTs, which exhibit very similar temporal response. The LII signal is recorded by an oscilloscope (Agilent Technologies DSO7034B, 350 MHz) and transferred to a PC for further treatment. Using gated PMTs, saturation of the PMTs due to flame luminosity between LII laser pulses can be avoided. The PMT gate was on for 1.3  $\mu\text{s}$  and the LII pulse is located 380 ns after gate opening. The CARS laser pulse is timed 1  $\mu\text{s}$  after the LII pulse, just after the PMT gate is off again.

Simultaneously, the 2D prompt LII signal is recorded with a gate of 20 ns on the opposite side of the combustor with an image intensified dual frame CCD camera (Dicam Pro, PCO) equipped with a 105-mm  $f/2.5$  camera lens (Nikon) and an appropriate band pass filter (LOT, 450FS40-50). This primarily serves monitoring the highly intermittent soot presence in the measurement volume of the time-resolved LII signal and identify correct operation of the system. Beyond that it allows for additional verification of the measurement position of the point diagnostics (TiRe LII and CARS) relative to the extension of a soot cloud. Quantitative 2D monitoring of the soot volume fraction, however, is not accessible by this setup since the short focal lengths excitation optics prevents a sufficiently homogeneous sheet thickness along the path through the combustor. That was not the goal of the experimental setup since this information had already been measured previously [17].

### 3.3 CARS-specifics

The CARS excitation scheme, specifically developed for sooting flames has been presented in [36] and used following several updates of components since [18, 37, 38].

According to [36], soot presence does not impact the derived temperatures with the employed excitation scheme. A frequency doubled Nd:YAG laser (Spectra Physics G290) with a repetition rate of 10 Hz ( $\lambda = 532$  nm, pulse duration  $\sim 8$  ns) was used to pump two dye lasers (Sirah Double Dye PrecisionScan): a narrowband dye laser was tuned to produce 591 nm (orange color), which provided the pump and probe beams (50% split). On the other hand, the broadband dye laser (Stokes beam) was set to peak around 685 nm (red color) with a bandwidth of about 10 nm. This choice of specific wavelengths shifts the CARS signal to 519 nm, hence avoiding signal interference due to laser-induced  $\text{C}_2$  emissions, a problem often encountered in sooting flames [36]. To obtain high-intensity CARS signal while maintaining high spatial resolution, a folded BOXCARs configuration [39] was used to achieve the necessary phase matching required for generating coherent CARS signal beam. Outside the CARS laser container the three laser beams (pump, Stokes and probe) were relayed by a series of high-reflectivity mirrors to the measurement position, focused by the above-mentioned  $f = 250$ -mm lens. Spatial resolution was determined to be  $< 0.1$  mm in diameter (using the beam profiling camera) and about 1.5 mm (L95%) in the laser beam propagating direction using the non-resonant CARS signal from a thin quartz plate placed at the measurement position. At the crossing point of the three laser beams, the 519 nm CARS anti-Stokes signal beam was generated, which traveled coherently in the same direction as the other laser beams. The currently used receiver optics consists of a collimation lens ( $f = 350$  mm) and a set of dichroic mirrors to spectrally separate the signal beam from the excitation lasers in the visible and infrared. Signal detection followed spectral dispersion in a spectrometer (Horiba, THR1000, 1200 lines/mm) using a 16-bit ICCD (Lavision, Nanostar).

Overlap of the CARS focus and the LII sheet was validated with a beam profiler (WinCam D) outside the pressure housing in a location representative of the measurement location inside the combustor. Furthermore, a target consisting of a pinhole and a thin quartz plate was used to check the overlap of all laser beams. Temporally, both diagnostics have been delayed to each other to avoid interferences. The CARS laser pulses were fired 1  $\mu\text{s}$  after the LII pulse. This ensures that the LII process is completely finished before the CARS process related to high laser power density (and consequently changes of the soot) starts. Given the known flow velocities [20] it can be estimated that this short delay does not yield an exchange of the mapped fluid elements between the laser pulses. Heat-up of the direct ambience of soot particles due to heat dissipation of the absorbed LII laser energy is neglected when interpreting the CARS temperatures. Such effect is expected not to exceed about 50 K for our studied conditions, in magnitude depending on the used LII fluence and soot concentrations [34].

## 4 Data evaluation

### 4.1 TiRe LII data evaluation

The measured instantaneous LII decay traces were first filtered to include only those pulses with sufficient signal level. Data evaluation was done using LIISim for the time-resolved LII signal [40]. Temperature traces were then calculated for each laser pulse. The background temperature was determined by averaging 200 ns of the temperature trace before the LII laser pulse. The parameter implementation for fitting the LII signal followed that by Kock, detailed in [33, 41], i.e. heat transfer model and material constants were used as reviewed in Appendix B of [40]. Variation of the gas composition only showed minor effect on the derived particle size. Therefore 100% nitrogen was used as the gas mixture, as nitrogen is the main component of the gas mixture. Temperature traces were fitted 20 ns after the peak to exclude the region where vaporization of the particles may take place. Decay rates were determined using the same fitting window by fitting a mono-exponential decay trace to the data.

The parameterization in LIISim does not account for polydispersity of the primary particle distribution (which is unknown anyways). Following respective statements in the excellent review on LII [42], based on detailed evaluation in [43], the LII decay behavior sensitively depends on a realistic description of polydispersity. Given the very short derived signal decay, however, we expect aggregation to be minor, thus leaving the polydispersity of primary particles as more significant factor. Additional uncertainty evolves from the insufficiently known soot properties under the studied conditions. Soot maturity, which is known to affect the optical properties of soot relevant for the LII process, can be traced in laminar flames [44], even if pressurized [45], under consideration of the involved uncertainties in the respective parameters (soot heat capacity, density, thermal accommodation coefficient,

to name few). However, that is not yet possible for turbulent cases. Therefore, the derived particle sizes can only provide a rough indication, hence are not to be mistaken as exact values.

### 4.2 CARS data evaluation

For CARS data analysis the in-house code CARSpy [46] was used. Prior to fitting the experimentally obtained spectra, the pixel axis was converted to wavelength (spectral) axis. For this, emission from a mercury-argon lamp (Avaspec) was coupled into the spectrometer using the same fiber optic used for CARS signal. In the spectral range of  $520 \pm 5$  nm, four strong argon atomic lines from the Ar-I system (516.2285 nm, 518.7746 nm, 522.1271 nm, 525.2788 nm) were used to determine the pixel-to-wavelength conversion. This calibration not only allows associating the CARS spectra with absolute wavelengths but also sets the correct dispersion of the spectral system, both of which are necessary for the spectral fitting. In addition, a tungsten lamp was used to create a flat background profile to correct for any wavelength-dependent quantum yield (signal intensity) of the spectrometer as well as the camera.

Each set of typically 1200 recorded CARS spectra was accompanied by a background spectrum that was acquired right after the CARS spectra and by blocking the laser beams. Pure Argon flow was used prior to the flame measurements to obtain the spectral profile of the broadband Stokes beam, which directly affects the profile of the CARS signal. In the end, each CARS spectrum prior to a fitting procedure was (1) subtracted by the background noise, (2) corrected for non-uniformities in the Stokes profile and (3) converted to a wavelength (wavenumber) axis.

In addition, the pump laser profile as well as the slit function of the spectrometer necessary for carrying out the spectral fitting was derived based on room air spectra as seen in Fig. 4.

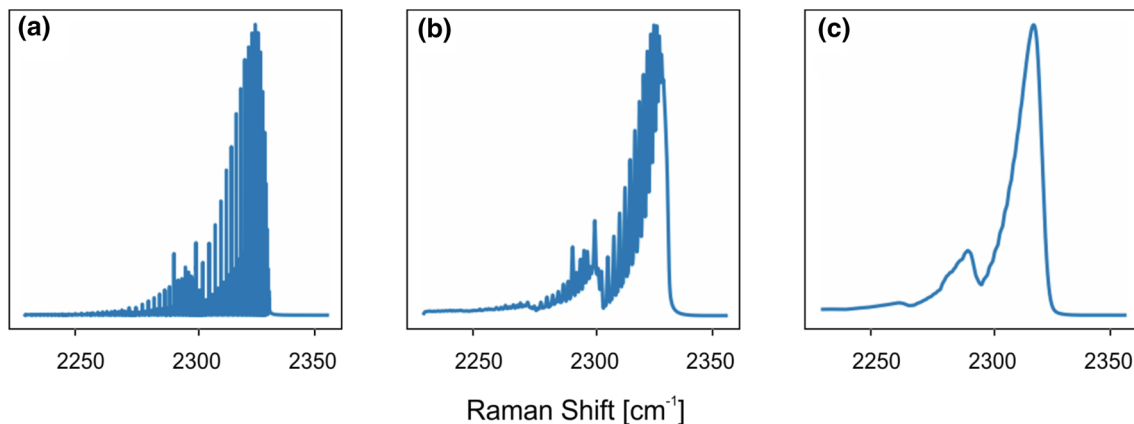


**Fig. 4** Synthetic CARS spectrum: **a** theoretical spectrum **b** influence from laser profile **c** influence from slit function, at 1 bar and 2000 K in air

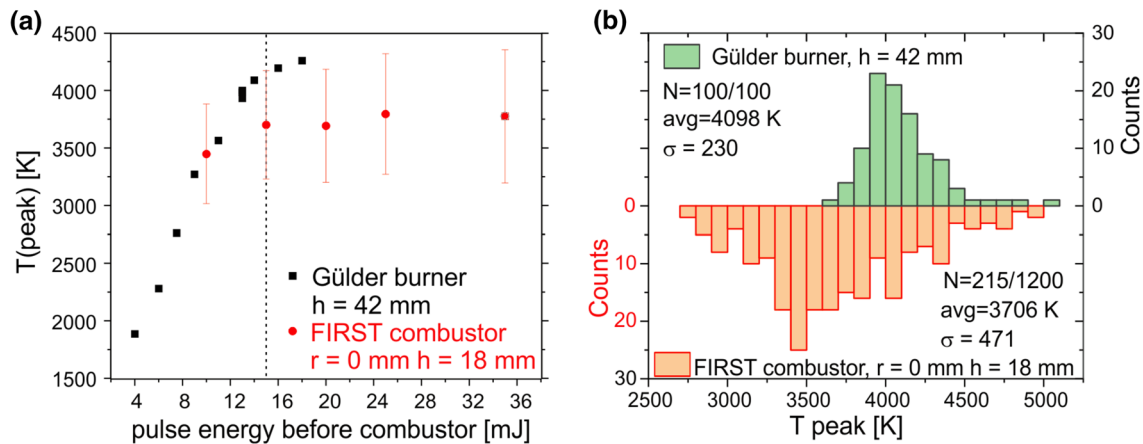


**Fig. 5** Fluence curves recorded for the Gülder flame and FIRST case (a) and distribution of peak temperatures (b) at the pulse energy indicated by a dashed line in the left plot

Experimental spectra were then fitted iteratively against theoretical ones using a least-square fitting routine. The fitting parameters included temperature ( $T$ ) and the ratio between  $N_2$  number density and the non-resonant background (which depends on the local gas composition and is usually unknown). Systematic errors may arise due to the treatment of the non-resonant background. Nevertheless, it has been shown in literature that such fitting could still provide fairly reliable temperature measurements [39]. Given the non-premixed nature in many measurement locations, alternative methods such as calculating theoretical non-resonant background by assuming local equilibrium may result in significant errors in premixing zones of the flame.

## 5 Results and discussion

For time-resolved LII, the chosen laser fluence in the measurement location is recommended to be below the LII threshold regime to avoid non-negligible surface sublimation. Therefore, we have recorded fluence curves for the laminar diffusion flame as well as for the turbulent pressurized target case. Since an access to inside the combustor could not be realized, the pulse energy before the experiment is plotted instead of the conventionally recommended exact fluence at the measurement location. The resulting curves are shown in Fig. 5a.

For the laminar flame, the expected peak temperature plateau is reached at about 4000 K. In the turbulent test case, a similar levelling-off trend is identified in the same fluence range. However, the peak temperature values were measured to be significantly lower. This drop of peak temperature under turbulent, pressurized conditions is attributed to a deterioration of the LII sheet quality in the measurement location due to beam steering, in addition to the more

pronounced conductive heat transfer. Fluctuating deterioration of the beam quality in the measurement location translates into a fluctuation of local laser fluence (i.e.  $x$ -axis, hot spots versus beam divergence) and a subsequent impact on peak temperatures on an instantaneous basis (i.e.  $y$ -axis), while the plot represents the resulting averages. The respective distributions of peak temperature for a pulse energy of roughly 15 mJ are shown in Fig. 5b, which indicates a significant widening of the distribution and decrease of temperature values for the turbulent case. The rate of valid LII laser pulses depended on soot presence, which was 100% out of 100 individual laser pulses for the laminar flame, and significantly lower for the turbulent flame due to soot intermittency, i.e. roughly 18% of the used 1200 pulse pairs for the given location. For other locations in the flames, and during different runs with the same conditions, we unfortunately have exported individual temperatures and therefrom deduced the standard deviation only for one location and value of laser energy; for the other energies, only the average was evaluated on-the-fly and recorded, thus a standard deviation is not available for those for further comparison.

When using appropriate fluence values, we achieve temperature decay curves as exemplarily shown in Fig. 6. It is evident that the temperature decay is significantly shorter for the pressurized case compared to the atmospheric one, which is partly due to the increased heat conduction with the pressure scaled by a factor of three, but more so by the significantly different particle sizes, which are very tiny for the turbulent pressurized flame. Our reference size for the well-characterized Gülder flame (standard location on-axis at 42 mm above the pipe exit) we derive roughly 18 nm particle size, which is lower than the value of 28.3 nm determined by TEM in [47]. This value served to refine the parameters used in F. Liu's model, as referenced in [40]. It is known that the parameterization by Kock yields somewhat smaller primary

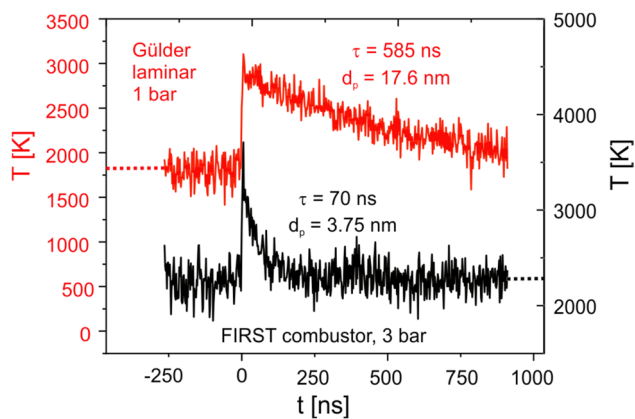


**Fig. 6** Comparison of individual temperature decay curves for the turbulent pressurized case relative to the laminar atmospheric flame

particle sizes compared to that by Liu (see application cases in [40]), therefore we evaluate the derived size range for our reference flame measurement as acceptable for the purpose of this study, i.e. derivation of relative information between the cases.

An impression of a subseries of LII recordings in a representative location of the turbulent pressurized flame ( $r=0$  mm,  $h=18$  mm) is shown in Fig. 7. Plot (a) of this figure shows a time trace of LII intensity for this position recorded by the ICCD and the PMT system, respectively. The time trace visualizes the intermittency of soot presence in the PMT detection volume of roughly 1 mm in diameter. LII signal in 2D representation and LII signal decay curve, already calibrated to temperature, are shown in panels (b) to (f). The location of the PMT measurement volume is labelled in the 2D plots. Different peak temperature is indicative of different energy transfer from the laser pulses to the soot particles in the measurement volume as detailed in Fig. 5b, due to beam steering or excitation with the wings of the laser sheet only. Panels (g) to (j) visualize individual situations where either no soot is present at all in the whole image, no soot filament is appearing more or less close to the PMT detection volume, or soot concentration in this volume is just insufficient to generate signal appropriate for calibration and detailed evaluation (j). For this last plot, Fig. 7a, j shows some non-background intensity which is, however, not producing enough signal to derive a particle size. It is evident that the decay time of all decay curves is quite similar as is the background temperature level.

The corresponding CARS spectra for some examples in Fig. 7 are shown in the following Fig. 8. Subplots (a) and (b) show an excellent fit quality in the higher and lower temperature range. The CARS fit in (c) is acceptable, however, due to insufficient soot signal for this instant (Fig. 7e), the data is not useful for the combined statistics. Figure 8d shows insufficient CARS fit quality (based on  $\chi^2$  values of the fit,

not shown in the plots) and is therefore discarded from the further analysis.

A typical instantaneous LII-derived temperature profile decay in the turbulent pressurized flame is shown in Fig. 9a. The trace covers the complete PMT gate. The temperature decay is significantly shorter than for the atmospheric Gülder flame (see Fig. 5). Unlike for the Gülder case, where the signal is long enough to select a suitable time window before background levels are reached, the fitting routine in LIIsim has to include the apparent temperature background to converge, which results in the solid red temperature trace. The apparent background, labelled with a blue dashed line however, is generated by naturally incandescing soot filaments at the measurement location (ideally) or between there and the detector, i.e. by any hot soot cloud in the LII detection cone shown in Fig. 2. Consequently, the derived LII background temperature for those short decay times is typically hotter than the instantaneously measured CARS temperature, on average shown in Fig. 9b. This effect is not to be mixed up with local heating of the ambience of soot particles due to absorption of laser energy during the LII process [34, 48, 49] for following reasons: (a) the analyzed LII temperature traces have roughly the same level behind compared to before the LII event, and (b) the soot concentrations are insufficient for significant local heating (up to 400 K for soot concentrations 30–40 times higher than in the present case [49]). Almost all instantaneously derived LII background temperatures show values in the narrow range of 2050 to 2250 K while the respective CARS temperatures cover a much wider range between 800 and 2300 K in the same locations (not shown).

To compensate for this within LIIsim without going through the exercise of creating an own fitting routine (only based on the first 100 ns and the final CARS temperature value) and adding an LII module to derive particle size, we have vertically shifted the individual temperature profiles such that the background temperature matches that of the corresponding CARS laser pulse. As a result of this practice, particle sizes increased by up to 12% when decreasing the temperature background level by 800 K to match the CARS temperature, which is considered non-negligible, yet without changing the derived sizes dramatically (Fig. 10a). To check the influence of this procedure, we also modified the spread of the individual temperature profiles according to Fig. 10b. That variation only showed negligible impact on the resulting particle size.

For further evaluation, only those TiRe LII pulses were considered for which a corresponding CARS spectrum of sufficient quality was available, i.e. the correction procedure for background temperature further reduced the statistics of soot particle sizes per location. This adds to the effect of soot intermittency which also reduces statistics from the initially acquired 1200 laser pulses per location. Major



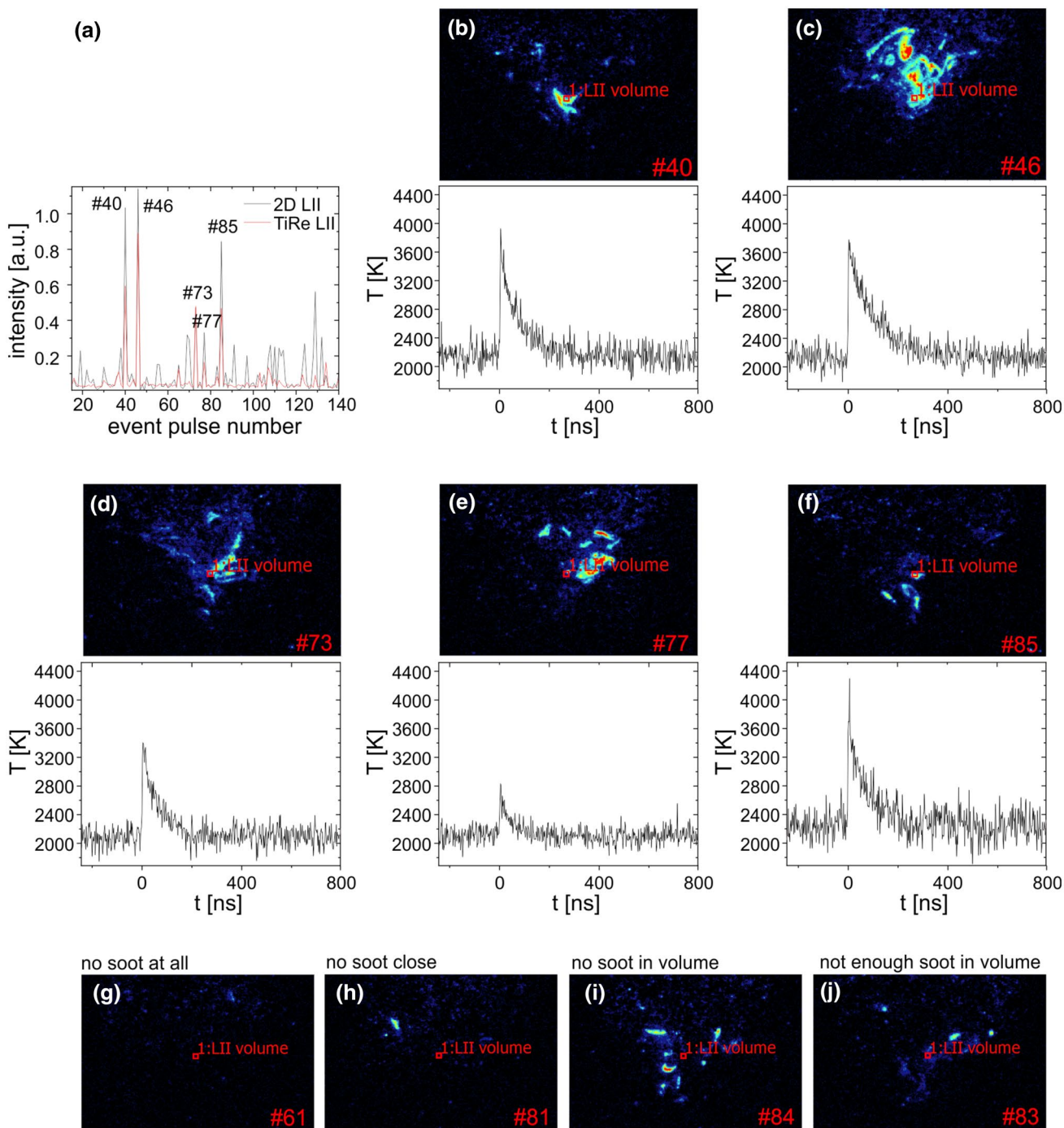


**Fig. 7** Local LII intensities in a measurement location at  $r=0$  mm and  $h=18$  mm in a selected subsequence (a) and pairs of 2D LII images and local temperature decay curves, translated from the LII

decay (b) to (f). Panels (g) to (j) show examples for the frequent situation of insufficient LII signal in the PMT detection volume

reason for insufficient CARS spectrum quality is the loss of overlap of the three CARS laser beams due to occasionally occurring pronounced thermal gradients in the flame, which then results in beam steering. The finally used number of laser pulses for derivation of primary particle size in various locations of the flame is shown on the left sub-panel of

Fig. 11a. Given the pronounced soot intermittency which is based on turbulence and time and composition histories of fluid elements, values of about 250 out of 1200 laser pulses can be considered quite high. In contrast, values below 100 are indicative of quite low statistics of the derived particle size. The resulting mean particle sizes are shown in the

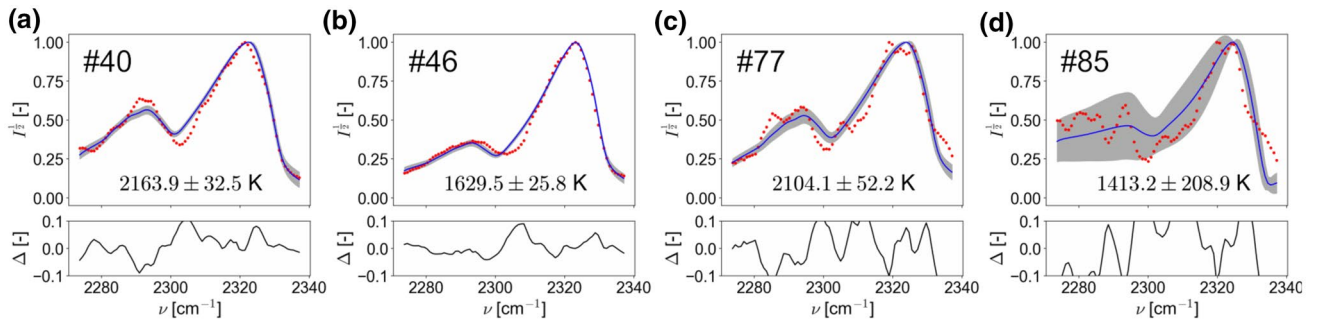


**Fig. 8** Local instantaneous CARS spectra and derived gas temperatures correlated to the LII events shown in Fig. 7b,c,e,f. Red dots: experiment, blue line: fit with gray uncertainty range

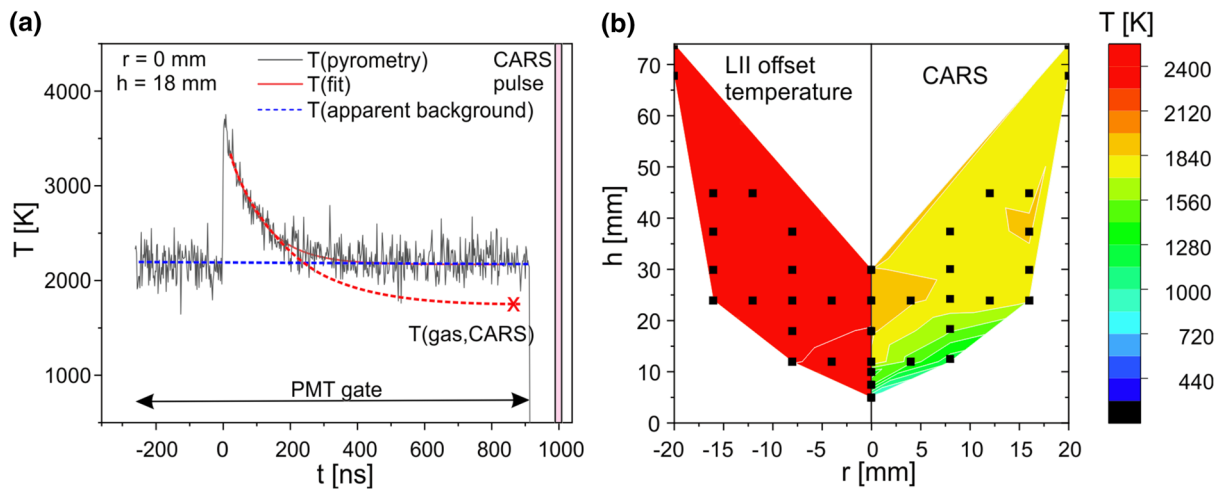


**Fig. 9** Instantaneous LII temperature decay during LII (a) in the turbulent pressurized flame; the different types of fit are explained in the text. (b) Comparison of LII offset and CARS temperatures

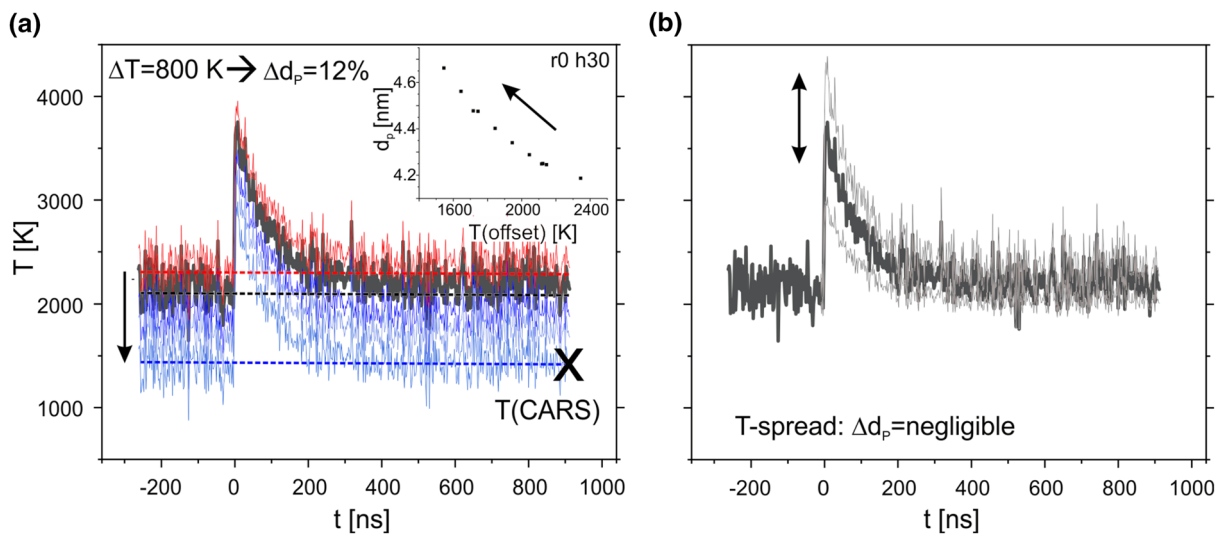


**Fig. 10** Schematic of the impact of modifying the LII derived temperature profiles to match CARS temperatures

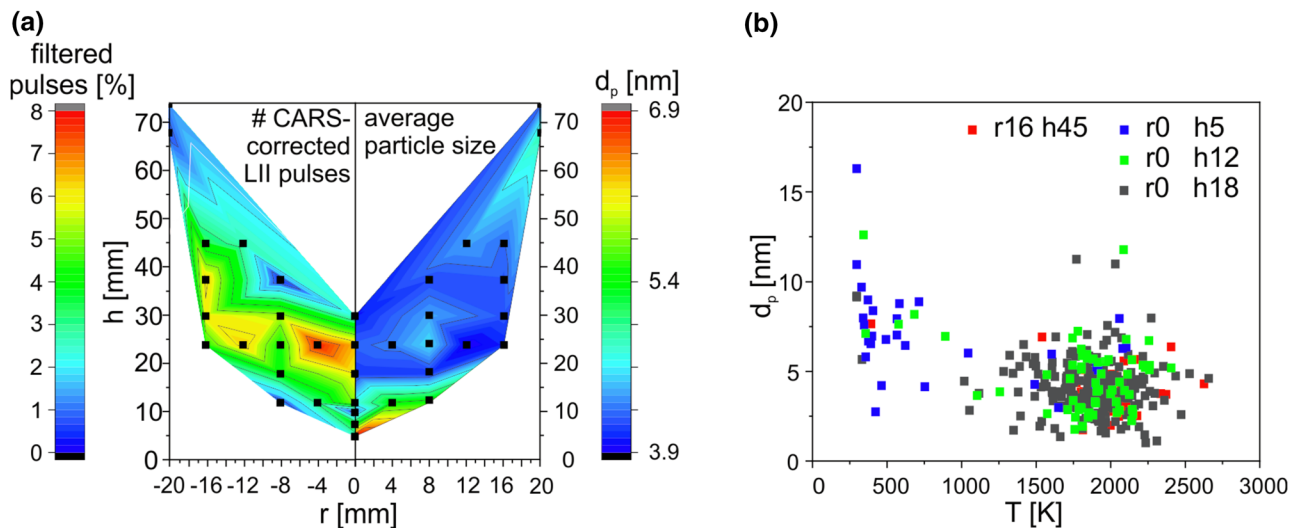


**Fig. 11** Number of CARS-corrected LII pulses per location and derived averaged primary particle sizes (a), and instantaneous correlation of CARS temperature with particle size (b)

right sub-panel of the same plot. Values are generally in the range of about 5 nm, i.e. far below the 25–30 nm reported for mature soot particles from laminar atmospheric flames with long residence times [47] or even after aircraft engines [50]. Our interpretation at current status is that the residence time in the characterized relatively weakly sooting flame are insufficient to form much larger particles. A correlation of particle sizes with local gas temperatures is shown in Fig. 11b. For three of the evaluated locations shown, no trend is visible, and the scatter of data points is grouped around 5 nm particle size in a temperature range between 1600 and 2400 K. At a height of 5 mm above the injector exit of the combustor several events show larger particle sizes at low temperatures. This location is situated below the stagnation point of the flow, i.e. in the cold inflow where the conditions are unfavorable for soot formation. Soot identified in this location is certainly transported there from downstream regions where formation can occur. This is generally plausible as transport through the low velocity inner recirculation zone into the inflow region increases the residence times of those fluid elements. However, soot growth is then quenched once the soot filaments enter those cold regions. It should be noted that large uncertainty of derived particle sizes and low statistics prevent identification of other clear trends with location.

Factors affecting the accuracy of determined particle sizes are lack of inclusion of particle polydispersity (unknown anyways), uncertainties of other soot properties on an instantaneous basis (characteristics of mapped soot vary from laser pulse to laser pulse), and signal noise, in addition to uncertainties induced by the fitting procedure of noisy, quickly decaying temperature traces. While local soot properties as

polydispersity or aggregation are inaccessible without availability of sampling, other properties depend on maturity, which is so far unmeasurable, specifically on an instantaneous level. More sophisticated signal analysis would allow for some improvement of the derived accuracy. However, we consider this outside the scope of the project where the general feasibility was focus of the research. Certainly, the collected data can be valuable to support soot modelling as good estimation of otherwise inaccessible information, and also serve as a basis to further optimize the diagnostics combination.

## 6 Conclusions

In this paper, we demonstrate a new diagnostics combination to non-intrusively determine in-flame particle sizes for a laminar and a turbulent pressurized case. The approach consists of combining time-resolved laser-induced incandescence (TiRe LII) and shifted vibrational coherent anti-Stokes Raman scattering (SV-CARS) and enables instantaneous evaluation of the primary particle size in a probe volume of roughly 1 mm in the length and few hundred micrometers in the width. CARS is employed to introduce the best available gas temperature into the evaluation of LII decay curves. An additional ICCD camera serves to monitor soot presence in the measurement volume. A first iteration using non-gated photomultiplier tubes failed due to too high flame luminosity. After implementation of gated devices, the signal quality was significantly improved. For given laser fluence used for LII excitation, the achieved peak temperatures of the LII process are significantly lower for the pressurized turbulent

flame which is attributed to increased heat conduction, and values show pronounced fluctuations, which is due to beam quality deterioration in the measurement volume (beam steering). Unlike in other configurations, the tail of the LII signal decay curve cannot be used to deduce the local gas temperature. Here, we have found clear evidence that this part of the signal curve is dominated by hot soot streaks present between the location of the laser excitation and the detection optics.

Determined particle sizes in the swirled pressurized sooting flame at 3 bar are consistently very small and in the range of 5 nm; the decay of particle temperature is significantly faster than for the laminar atmospheric flame used for reference. In the pressurized flame, only a small variation of primary particle size is identified, which is also relatively insensitive to moderate variations in equivalence ratio or omission of the secondary air injection. For one location indicative of cold inflow conditions where soot presence is a result of transport phenomena, soot particles are somewhat larger (exceeding 10 nm). Unfortunately, the measurements suffer from relatively poor statistics due to soot intermittency, which is the result of a compromise between operation times, and soot load affecting clearness of the combustor windows. Potentials for narrowing down current uncertainties exist, but are out of the scope of the current paper, which serves to demonstrate the principal approach.

**Acknowledgements** The authors acknowledge financial support via the European project Soprano, Grant Agreement No 690724.

**Author contributions** All authors jointly performed the experiment, discussed the results, and contributed to the figures. HS, PN and ZY realized the data evaluation. KPG, PN and ZY compiled and reviewed the manuscript.

**Funding** Open Access funding enabled and organized by Projekt DEAL.

**Data availability** Data can be made available upon request to the authors for further exploration or use for model validation.

## Declarations

**Competing interests** The authors declare no competing interests.

**Open Access** This article is licensed under a Creative Commons Attribution 4.0 International License, which permits use, sharing, adaptation, distribution and reproduction in any medium or format, as long as you give appropriate credit to the original author(s) and the source, provide a link to the Creative Commons licence, and indicate if changes were made. The images or other third party material in this article are included in the article's Creative Commons licence, unless indicated otherwise in a credit line to the material. If material is not included in the article's Creative Commons licence and your intended use is not permitted by statutory regulation or exceeds the permitted use, you will need to obtain permission directly from the copyright holder. To view a copy of this licence, visit <http://creativecommons.org/licenses/by/4.0/>.

## References

1. D.S. Lee, D.W. Fahey, A. Skowron, M.R. Allen, U. Burkhardt, Q. Chen, S.J. Doherty, S. Freeman, P.M. Forster, J. Fuglestedt, A. Gettelman, R.R. De Leon, L.L. Lim, M.T. Lund, R.J. Millar, B. Owen, J.E. Penner, G. Pitari, M.J. Prather, R. Sausen, L.J. Wilcox, The contribution of global aviation to anthropogenic climate forcing for 2000 to 2018. *Atmos. Environ.* **244**, 117834 (2021)
2. D. Jacob, T. Rindlisbacher, The landing and take-off particulate matter standards for aircraft gas turbine engines, ICAO Environmental Reports, Chapter Three: Local Air Quality, ICAO, 2019, pp. 100–105.
3. L. Gallen, A. Felden, E. Riber, B. Cuenot, Lagrangian tracking of soot particles in LES of gas turbines. *Proc. Combust. Inst.* **37**, 5429–5436 (2019)
4. M. Grader, C. Eberle, P. Gerlinger, M. Aigner, LES of a pressurized, sooting aero-engine model combustor at different equivalence ratios with a sectional approach for PAHs and soot, Proc. ASME Turbo Expo, 2018, GT2018–75254.
5. R. Mansmann, T. Dreier, C. Schulz, Performance of photomultipliers in the context of laser-induced incandescence. *Appl. Opt.* **56**, 7849–7860 (2017)
6. D.R. Snelling, G.J. Smallwood, F. Liu, O.L. Gülder, W.D. Bachalo, A calibration-independent laser-induced incandescence technique for soot measurement by detecting absolute light intensity. *Appl. Opt.* **44**, 6773–6785 (2005)
7. R. Hedef, K.P. Geigle, J. Zerbs, R.A. Sawchuk, D.R. Snelling, The concept of 2D gated imaging for particle sizing in a laminar diffusion flame. *Appl. Phys. B* **112**, 395–408 (2013)
8. Z.W. Sun, D.H. Gu, G.J. Nathan, Z.T. Alwahabi, B.B. Dally, Single-shot, Time-Resolved planar Laser-Induced Incandescence (TiRe-LII) for soot primary particle sizing in flames. *Proc. Combust. Inst.* **35**, 3673–3680 (2015)
9. Y. Chen, E. Cenker, D.R. Richardson, S.P. Kearney, B.R. Halls, S.A. Skeen, C.R. Shaddix, D.R. Gueldenbecher, Single-camera, single-shot, time-resolved laser-induced incandescence decay imaging. *Opt. Lett.* **43**, 5363–5366 (2018)
10. M. Bouvier, J. Yon, F. Liu, G. Cabot, F. Grisch, Application of planar auto-compensating laser-induced incandescence to low-sooting turbulent flames and investigation of the detection gate width effect. *Aerosol Sci. Technol.* **55**, 1215–1229 (2021)
11. B. Tian, C. Zhang, Y. Gao, S. Hochgreb, Planar 2-color time-resolved laser-induced incandescence measurements of soot in a diffusion flame. *Aerosol Sci. Technol.* **51**, 1345–1353 (2017)
12. M. Hofmann, F. Kock, T. Dreier, H. Jander, C. Schulz, Laser-induced incandescence for soot-particle sizing at elevated pressure. *Appl. Phys. B* **90**, 629–639 (2008)
13. X.T. Mi, A. Saylam, T. Endres, C. Schulz, T. Dreier, Near-threshold soot formation in premixed flames at elevated pressure. *Carbon* **181**, 143–154 (2021)
14. F.S. Liu, D.R. Snelling, G.J. Smallwood, Numerical study of temperature and incandescence intensity of nanosecond pulsed-laser heated soot particles at high pressures, Proc. ASME IMECE, 2005, IMECE2005–81322.
15. E. Cenker, G. Bruneaux, T. Dreier, C. Schulz, Sensitivity analysis for soot particle size imaging with laser-induced incandescence at high pressure. *Appl. Phys. B* **119**, 745–763 (2015)
16. D.H. Gu, Z.W. Sun, B.B. Dally, P.R. Medwell, Z.T. Alwahabi, G.J. Nathan, Simultaneous measurements of gas temperature, soot volume fraction and primary particle diameter in a sooting lifted turbulent ethylene/air non-premixed flame. *Combust. Flame* **179**, 33–50 (2017)
17. K.P. Geigle, R. Hedef, W. Meier, Soot formation and flame characterization of an aero-engine model combustor burning ethylene

- at elevated pressure. *J. Eng. Gas. Turbines Power* **136**, 021505 (2014)
18. K.P. Geigle, M. Köhler, W. O'Loughlin, W. Meier, Investigation of soot formation in pressurized swirl flames by laser measurements of temperature, flame structures and soot concentrations. *Proc. Combust. Inst.* **35**, 3373–3380 (2015)
  19. K.P. Geigle, W. O'Loughlin, R. Hadeef, W. Meier, Visualization of soot inception in turbulent pressurized flames by simultaneous measurement of laser-induced fluorescence of polycyclic aromatic hydrocarbons and laser-induced incandescence, and correlation to OH distributions. *Appl. Phys. B* **119**, 717–730 (2015)
  20. K.P. Geigle, R. Hadeef, M. Stöhr, W. Meier, Flow field characterization of pressurized sooting swirl flames and relation to soot distributions. *Proc. Combust. Inst.* **36**, 3917–3924 (2017)
  21. M. Stöhr, K.P. Geigle, R. Hadeef, I. Boxx, C.D. Carter, M. Grader, P. Gerlinger, Time-resolved study of transient soot formation in an aero-engine model combustor at elevated pressure. *Proc. Combust. Inst.* **37**, 5421–5428 (2019)
  22. I. Litvinov, J. Yoon, C. Noren, M. Stöhr, I. Boxx, K.P. Geigle, Time-resolved study of mixing and reaction in an aero-engine model combustor at increased pressure. *Combust. Flame* **231**, 111474 (2021)
  23. P. Nau, Z. Yin, K.P. Geigle, W. Meier, Wall temperature measurements at high pressures and temperatures in sooting flames in a gas turbine model combustor. *Appl. Phys. B* **123**, 279 (2017)
  24. G.J. Nathan, International Sooting Flame (ISF) Workshop. <https://www.adelaide.edu.au/cet/isfworkshop/about-isf>. Accessed 05 Jan 2023
  25. C. Eberle, P. Gerlinger, M. Aigner, A sectional PAH model with reversible PAH chemistry for CFD soot simulations. *Combust. Flame* **179**, 63–73 (2017)
  26. N. Dellinger, Modélisation de la formation et de l'évolution des particules de suie en approche hybride Euler-Lagrange pour la simulation de foyers aéronautiques, PhD Thesis, Sorbonne Université, 2019.
  27. P. Rodrigues, Modélisation multiphysique de flammes turbulentes suivies avec la prise en compte des transferts radiatifs et des transferts de chaleur pariétaux, PhD Thesis, Université Paris-Saclay, 2018.
  28. L. Gallen, Prediction of soot particles in Gas Turbine Combustors using Large Eddy Simulation, PhD Thesis, Institut National Polytechnique de Toulouse, 2020.
  29. M. Grader, Large-Eddy Simulation und Analyse turbulenter, rußender Flammen, PhD Thesis, University Stuttgart, 2023.
  30. D. Galley, S. Ducruix, F. Lacas, D. Veynante, Mixing and stabilization study of a partially premixed swirling flame using laser induced fluorescence. *Combust. Flame* **158**, 155–171 (2011)
  31. A. Karmarkar, S. Gupta, I. Boxx, S. Hemchandra, J. O'Connor, Impact of precessing vortex core dynamics on the thermoacoustic instabilities in a swirl-stabilized combustor. *J. Fluid Mech.* **946**, A36 (2022)
  32. Ö.L. Gülder, D.R. Snelling, R.A. Sawchuk, Influence of hydrogen addition to fuel on temperature field and soot formation in diffusion flames. *Proc. Combust. Inst.* **26**, 2351–2358 (1996)
  33. C. Schulz, B.F. Kock, M. Hofmann, H. Michelsen, S. Will, B. Bougie, R. Suntz, G. Smallwood, Laser-induced incandescence: recent trends and current questions. *Appl. Phys. B* **83**, 333–354 (2006)
  34. E. Nordström, N.E. Olofsson, J. Simonsson, J. Johnsson, H. Bladh, P.E. Bengtsson, Local gas heating in sooting flames by heat transfer from laser-heated particles investigated using rotational CARS and LII. *Proc. Combust. Inst.* **35**, 3707–3713 (2015)
  35. F. Abou Nada, C. Knappe, M. Alden, M. Richter, Improved measurement precision in decay time-based phosphor thermometry. *Appl. Phys. B* **122**, 170 (2016). <https://doi.org/10.1007/s00340-016-6446-4>
  36. K.P. Geigle, Y. Schneider-Kühnle, M.S. Tsurikov, R. Hadeef, R. Lückerrath, V. Krüger, W. Stricker, M. Aigner, Investigation of laminar flames for soot model validation using SV-CARS and LII. *Proc. Combust. Inst.* **30**, 1645–1653 (2005)
  37. L. Cantu, J. Grohmann, W. Meier, M. Aigner, Temperature measurement in confined swirling spray flames by vibrational anti-Stokes Raman spectroscopy. *Exp. Therm. Fluid Sci.* **95**, 52–59 (2018)
  38. O. Lammel, K.P. Geigle, R. Lückerrath, W. Meier, M. Aigner, Investigation of soot formation and oxidation in a high-pressure gas turbine model combustor by laser techniques, *Proc. ASME Turbo Expo, 2007*, GT2007–27902.
  39. A.C. Eckbreth, *Laser Diagnostics for Combustion Temperature and Species* (CRC Press, Boca Raton, 1996)
  40. R. Mansmann, T. Terheiden, P. Schmidt, J. Menser, T. Dreier, T. Endres, C. Schulz, LIISim: a modular signal processing toolbox for laser-induced incandescence measurements. *Appl. Phys. B* **124**, 69 (2018)
  41. B. Kock, Zeitaufgelöste Laserinduzierte Inkandeszenz (TR-LII): Partikelgrößenmessung in einem Dieselmotor und einem Gasphasenreaktor, PhD Thesis, Duisburg-Essen, 2005.
  42. H.A. Michelsen, C. Schulz, G.J. Smallwood, S. Will, Laser-induced incandescence: Particulate diagnostics for combustion, atmospheric, and industrial applications. *Prog. Energy Combust. Sci.* **51**, 2–48 (2015)
  43. F. Liu, M. Yang, F.A. Hill, D.R. Snelling, G.J. Smallwood, Influence of polydisperse distributions of both primary particle and aggregate size on soot temperature in low-fluence LII. *Appl. Phys. B* **83**, 383–395 (2006)
  44. N.E. Olofsson, J. Simonsson, S. Torok, H. Bladh, P.E. Bengtsson, Evolution of properties for aging soot in premixed flat flames studied by laser-induced incandescence and elastic light scattering. *Appl. Phys. B* **119**, 669–683 (2015)
  45. M. Mannazhi, S. Torok, J.L. Gao, P.E. Bengtsson, Soot maturity studies in methane-air diffusion flames at elevated pressures using laser-induced incandescence. *Proc. Combust. Inst.* **38**, 1217–1224 (2021)
  46. Z. Yin, CARSPy: Synthesizing and fitting coherent anti-Stokes Raman spectra in Python GitHub Repository (2021) <https://github.com/chuckedfromspace/carspy>
  47. K. Tian, F.S. Liu, K.A. Thomson, D.R. Snelling, G.J. Smallwood, D.S. Wang, Distribution of the number of primary particles of soot aggregates in a nonpremixed laminar flame. *Combust. Flame* **138**, 195–198 (2004)
  48. D.R. Snelling, K.A. Thomson, F. Liu, G.J. Smallwood, Comparison of LII derived soot temperature measurements with LII model predictions for soot in a laminar diffusion flame. *Appl. Phys. B* **96**, 657–669 (2009)
  49. A.M. Bennett, E. Cenker, W.L. Roberts, Effects of soot volume fraction on local gas heating and particle sizing using laser induced incandescence. *J. Aerosol Sci.* **149**, 105598 (2020)
  50. D. Delhay, F.-X. Ouf, D. Ferry, I.K. Ortega, O. Penanhoat, S. Peillon, F. Salm, X. Vancassel, C. Focsa, C. Irimiea, N. Harivel, B. Perez, E. Quinton, J. Yon, D. Gaffie, The MERMOSE project: characterization of particulate matter emissions of a commercial aircraft engine. *J. Aerosol Sci.* **105**, 48–63 (2017)

**Publisher's Note** Springer Nature remains neutral with regard to jurisdictional claims in published maps and institutional affiliations.